Stress triggering in thrust and subduction earthquakes and stress interaction between the southern San Andreas and nearby thrust and strike-slip faults

Jian Lin
Department of Geology and Geophysics, Woods Hole Oceanographic Institution, Woods Hole, Massachusetts, USA

Ross S. Stein
U.S. Geological Survey, Menlo Park, California, USA

Received 30 May 2003; revised 24 October 2003; accepted 20 November 2003; published 3 February 2004.

[1] We argue that key features of thrust earthquake triggering, inhibition, and clustering can be explained by Coulomb stress changes, which we illustrate by a suite of representative models and by detailed examples. Whereas slip on surface-cutting thrust faults drops the stress in most of the adjacent crust, slip on blind thrust faults increases the stress on some nearby zones, particularly above the source fault. Blind thrusts can thus trigger slip on secondary faults at shallow depth and typically produce broadly distributed aftershocks. Short thrust ruptures are particularly efficient at triggering earthquakes of similar size on adjacent thrust faults. We calculate that during a progressive thrust sequence in central California the 1983 M_w = 6.7 Coalinga earthquake brought the subsequent 1983 M_w = 6.0 Nuñez and 1985 M_w = 6.0 Kettleman Hills ruptures 10 bars and 1 bar closer to Coulomb failure. The idealized stress change calculations also reconcile the distribution of seismicity accompanying large subduction events, in agreement with findings of prior investigations. Subduction zone ruptures are calculated to promote normal faulting events in the outer rise and to promote thrust-faulting events on the periphery of the seismic rupture and its downdip extension. These features are evident in aftershocks of the 1957 M_w = 9.1 Aleutian and other large subduction earthquakes. We further examine stress changes on the rupture surface imparted by the 1960 M_w = 9.5 and 1995 M_w = 8.1 Chile earthquakes, for which detailed slip models are available. Calculated Coulomb stress increases of 2–20 bars correspond closely to sites of aftershocks and postseismic slip, whereas aftershocks are absent where the stress drops by more than 10 bars. We also argue that slip on major strike-slip systems modulates the stress acting on nearby thrust and strike-slip faults. We calculate that the 1857 M_w = 7.9 Fort Tejon earthquake on the San Andreas fault and subsequent interseismic slip brought the Coalinga fault ~1 bar closer to failure but inhibited failure elsewhere on the Coast Ranges thrust faults. The 1857 earthquake also promoted failure on the White Wolf reverse fault by 8 bars, which ruptured in the 1952 M_w = 7.3 Kern County shock but inhibited slip on the left-lateral Garlock fault, which has not ruptured since 1857. We thus contend that stress transfer exerts a control on the seismicity of thrust faults across a broad spectrum of spatial and temporal scales. *INDEX TERMS:* 7209 Seismology: Earthquake dynamics and mechanics; 7230 Seismology: Seismicity and seismotectonics; 7223 Seismology: Seismic hazard assessment and prediction; 8164 Tectonophysics: Stresses—crust and lithosphere; 8123 Tectonophysics: Dynamics, seismotectonics; *KEYWORDS:* earthquake triggering, thrust and subduction earthquakes, stress transfer, fault interaction, blind thrust, San Andreas Fault

Citation: Lin, J., and R. S. Stein (2004), Stress triggering in thrust and subduction earthquakes and stress interaction between the southern San Andreas and nearby thrust and strike-slip faults, *J. Geophys. Res.*, *109*, B02303, doi:10.1029/2003JB002607.

1. Introduction

[2] During the past decade, the phenomenon of static stress transfer has been explored to understand earthquake interaction. Most studies have focused on earthquakes on strike-slip faults, such as the San Andreas, North Anatolian, and eastern California shear zone; or on normal faults in western Turkey, Greece, Italy, and the U.S. basin and range province (see reviews by *Harris* [1998], *Stein* [1999], *King and Cocco* [2000], and *Stein* [2003]). One advantage of studying strike-slip earthquakes is that the pattern of stress

0148-0227/04/2003JB002607$09.00

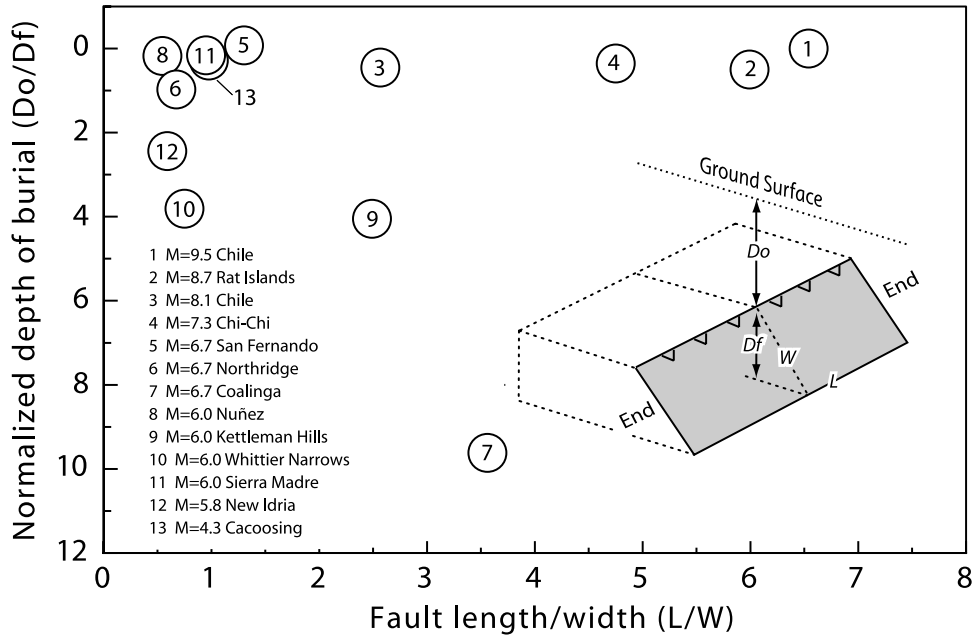

Figure 1. Depth of burial as a function of fault length/width (*L/W*) ratio for some well-studied thrust faults. Burial depth is normalized by the vertical extent of the fault, as shown in the inset. Large subduction earthquakes tend to locate in the upper right; moderate size continental thrust faults tend to locate to the left. Sources are 1, *Barrientos and Ward* [1990]; 2, *Lay et al.* [1989]; 3, *Ihmle and Ruegg* [1997]; 4, *Wang* [2000]; 5 and 6, *Stein et al.* [1994]; 7, 8, and 12, *Stein and Ekström* [1992]; 9, *Ekström et al.* [1992]; 10, *Lin and Stein* [1989]; 11, *Hauksson* [1994]; 13, *Seeber et al.* [1998].

transfer does not vary greatly with depth, so one can use aftershocks to test the predicted distribution of off-fault stress changes despite their large depth uncertainties. Conversely, the majority of thrust events occur in subduction zones offshore, where seismic and geodetic coverage is often poor.

[3] Despite these limitations, thrust faults are a tantalizing target of study: Thrust earthquakes have been responsible for most of the 20th century's seismic fatalities and financial losses, and thrust faults pose a major hazard to urban centers in California, the Pacific Northwest, Central and South America, Japan, India, Iran, and Taiwan. Unlike strike-slip systems, thrust faults are often "blind," meaning that the fault does not reach the Earth's surface, which profoundly alters the stress transfer. Previous investigations of continental thrust events [*Stein et al.*, 1994; *Harris et al.*, 1995; *Deng and Sykes*, 1997; *Hardebeck et al.*, 1998; *Wang and Chen*, 2001; *Wang et al.*, 2003] and subduction earthquakes [*Dmowska et al.*, 1988; *Taylor et al.*, 1996, 1998; *Parsons*, 2002] pointed to the important role of stress interaction. However, the common features of stress transfer in thrust systems are still poorly understood. Progress in understanding of this process should improve our ability to forecast earthquake hazards.

[4] Here we explore how thrust events interact, cluster, propagate, and inhibit each other. We first present a suite of idealized models illustrating the key features of Coulomb stress transfer associated with blind and surface cutting thrust faults. We then show how these models capture much of the observed aftershock distributions of continental thrust and subduction events, and can rationalize several propagating earthquake sequences. Finally, we explore how thrust and strike-slip faults are influenced by the stresses transmitted by a nearby major transform system, focusing on interaction between the San Andreas fault and the Coast Ranges faults. Although time-dependent stress transfer associated with viscous flow is important [*Pollitz and Sacks*, 1997; *Freed and Lin*, 1998; *Casarotti and Piersanti*, 2003], here we will focus on elastic processes that dominate coseismic stress changes. Where necessary we also use simplified dislocation models to examine interseismic stress accumulation.

2. Idealized Models of Stress Transfer

2.1. Surface-Cutting Faults Versus Blind Thrust Faults

[5] The degree of blindness of thrust faults varies over a broad spectrum (Figure 1), as surveyed by *Lettis et al.* [1997]. For blind thrusts with normalized depth of burial <1, such as the 1971 M_w = 6.7 San Fernando earthquake, the pattern of Coulomb stress is strongly influenced by the stress-free ground surface. The Coulomb stress change is defined as $\Delta CFF = \Delta\tau + \mu\Delta\sigma$, where $\Delta\tau$ is the change in shear stress (positive in the slip direction), $\Delta\sigma$ is the change in normal stress (positive when the fault is unclamped), and μ is the apparent friction coefficient after accounting for the pore fluid pressure effect, which is sometimes represented as μ' [*King et al.*, 1994]. A thrust fault that cuts the entire brittle-elastic layer of the crust relieves stress over a broad area in its cross-sectional area, inhibiting failure on nearby thrust faults (Figure 2a). In contrast, blind thrust faults increase the stress toward failure in a much larger percentage area of their immediate vicinity, including the overlying crust (Figure 2b). Blind thrusts can thus trigger relatively

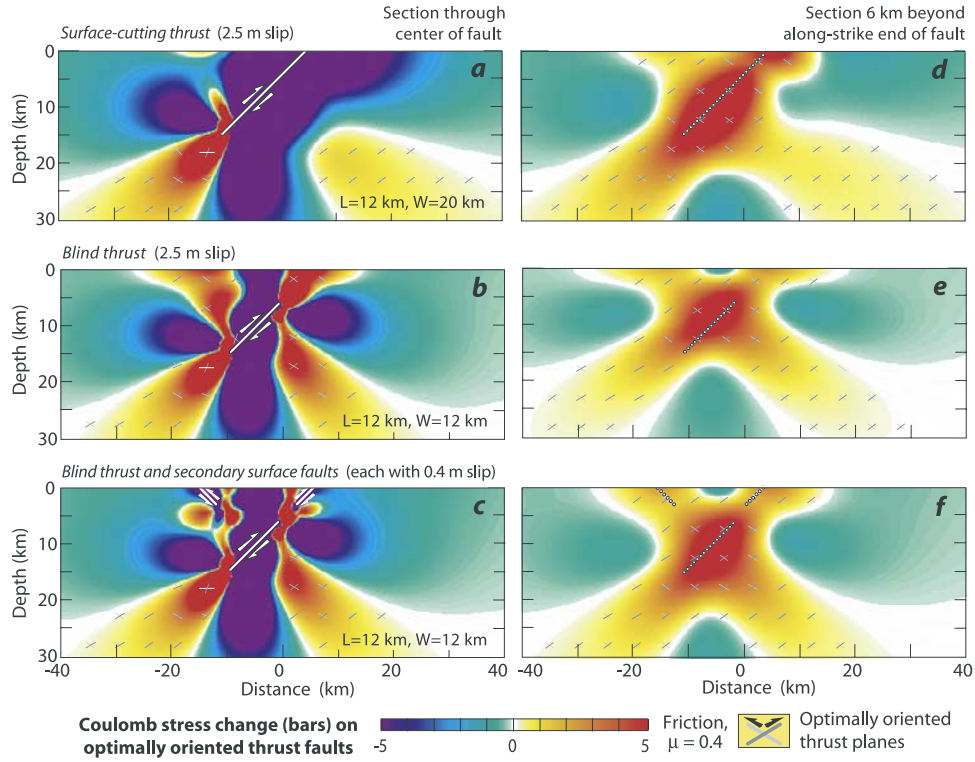

Figure 2. Cross sections (left) through the center and (right) beyond the end of the fault of a 45°-dipping thrust source fault. Optimally oriented receiver thrust planes are shown in areas of increased Coulomb stress. Both the 1971 San Fernando and 1994 Northridge faults dip about 45°. (a) The surface-cutting thrust (M_w = 7.0) drops the stress in the upper crust, (b) whereas a blind thrust (M_w = 6.8) increases the stress over much of the upper crust, despite its smaller magnitude. Near-surface regions of stress increase are sometimes relieved by secondary surface faulting, as occurred in the Northridge shock. (c) Stress changes caused by blind and surface fault slip. (d–f) Beyond the ends of the faults the stress distribution is relatively insensitive to whether the thrust is surface-cutting or blind, where the along-strike projection of faults is dotted.

abundant off-fault seismicity, including aftershocks or subsequent main shocks.

[6] The stress imparted by a blind thrust earthquake to the overlying crust is often relieved by secondary surface faults (Figure 2c). Secondary surface faulting is evident in the 1994 M_w = 6.7 Northridge earthquake [*Stein et al.*, 1994], and rootless secondary thrust faults are imaged in the cores of anticlines (upwarped strata) above the 1983 Coalinga and 1985 Kettleman Hills thrust events [*Stein and Ekström*, 1992]. However, existing bedding planes within sedimentary strata may significantly inhibit upward propagation of a thrust fault, and thus influence stress transfer [*Roering et al.*, 1997]. Stress that promotes reverse faulting is also transferred along the strike, beyond the ends of the rupture (Figures 2d–2f; see Figure 1 inset for terminology). The calculated off-fault stress increases exhibit a broad cross in cross section, and so aftershocks beyond the fault ends should also be widely dispersed, rather than aligned with the earthquake rupture plane.

[7] The diffuse pattern of aftershocks for blind thrust main shocks is evident in numerous well-documented examples, such as the 1983 Coalinga and 1985 Kettleman Hills [*Stein and Ekström*, 1992], 1987 M_w = 6.0 Whittier Narrows [*Shearer*, 1997], and 1994 Northridge [*Hardebeck et al.*, 1998] earthquakes. The Whittier Narrows earthquake, for example, is so deeply buried that there is no influence of the ground surface, and its aftershock distribution is highly compact (Figure 3). Although aftershocks close to the rupture plane are probably triggered by stress concentrations arising from discontinuities along the fault surface that are not represented by our smooth slip models, the off-fault shocks appear to lie in regions that sustained a Coulomb stress increase (Figures 3a and 3b), or were unclamped (Figure 3c).

[8] The correspondence between the off-fault aftershocks and the calculated unclamping for the Whittier Narrows earthquake (Figure 3c) suggests that aftershocks of thrust faults are sensitive to normal stress changes. Thus the apparent friction coefficient μ in the Coulomb stress equation would appear to be high for thrust faults, perhaps about 0.8. This inference has also been made for other thrusts and for strike-slip faults with little cumulative slip, perhaps because youthful fault surfaces are rough [*Parsons et al.*, 1999; *Toda and Stein*, 2003]. In contrast, evidence favors low friction for strike-slip faults with significant cumulative slip, such as the San Andreas, for which $\mu < 0.4$ [*Zoback et al.*, 1987; *Harris et al.*, 1995; *Parsons et al.*, 1999; *Toda and Stein*, 2002]. Subduction zones likely have intermediate friction because of large cumulative slip and the likelihood of high pore pressure. So here we will use μ = 0.8 for

continental thrusts, but $\mu = 0.4$ for subduction zones, major strike-slip faults, and schematic examples.

[9] There are several ways to calculate the Coulomb stress imparted by an earthquake, and we will use two in this study. The Coulomb stress can be resolved on to particular planes in a specified rake direction, known as "receiver faults." We use such specified-fault calculations when the geometry and rake of the receiver fault is known, such as in a sequence of large thrust earthquakes. When examining the correspondence between the earthquake stress change and small aftershocks, however, the faults on which most aftershocks occur are unknown. In such cases, we calculate the stress changes on optimally oriented faults. In other words, at every point in space, the plane on which the Coulomb stress change is most positive is found [*King et al.*, 1994]. Figure legends of all figures that show stress calculations detail which type of calculation is made.

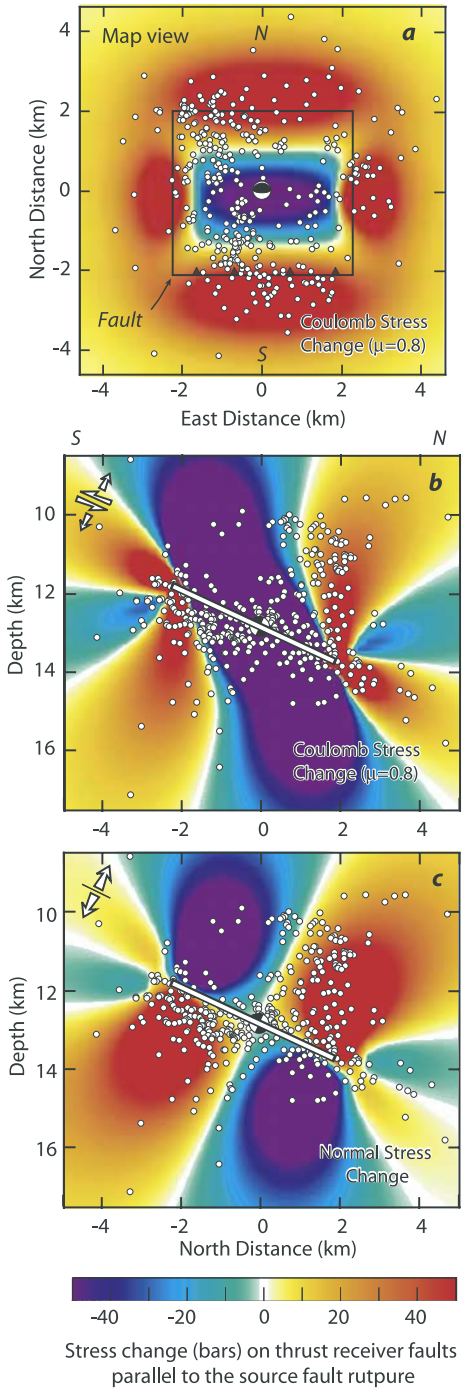

2.2. Interaction on Short Versus Long Thrust Faults

[10] When thrust earthquakes grow to $M \geq 7$ they often become longer along strike than they are wide in the downdip direction, because their downdip extent is limited by the finite depth of the brittle-elastic crust. In such cases, the stress transferred beyond the along-strike ends remains similar to that of short faults (Figure 4a), but the regions of stress decrease located perpendicular to the fault strike grow broader along strike (Figure 4b). Figures 4 and 5 display the same cases in map view and cross section, respectively.

[11] It has often been noted that, unlike strike-slip events, great subduction earthquake sequences more rarely propagate along strike [*Ruff and Tichelaar*, 1996]. The ability of a thrust earthquake to promote failure on an adjacent patch of similar size is strongly influenced by its length/width (L/W) ratio. For a square fault with 2 m of slip, about 70% of the adjacent patch experiences a stress increase of 1 bar or more (Figure 6a). For a fault of the same slip but with $L/W \sim 6$, only 15% of the adjacent patch sustains a 1-bar stress increase (Figure 6b). The Middle America subduction zone tends to rupture in $M < 7.4$ earthquakes with $L/W \sim 1$, whereas the Aleutian and Chilean subduction zones more commonly rupture in $M \geq 8$ earthquakes with $L/W > 3$. Thus short continental thrust faults and $M < 7.4$ subduction shocks should be more efficient at triggering subsequent earthquakes of similar size along strike than great subduction zone earthquakes.

[12] The ability of a subduction event to inhibit thrust faulting inland of the trench is similarly influenced by the L/W ratio. The zone of Coulomb stress decrease, known as the "stress shadow," is several times larger for the $L/W = 6$ case (Figure 6b) than for the $L/W = 1$ case (Figure 6a) because such areas of stress decrease grow broader along the strike of the rupture as L/W increases. Thus short thrust ruptures are efficient in triggering other thrust events of similar size along the strike of the rupture plane, while long

Figure 3. Stress change caused by the 1 October 1987 $M_w = 6.0$ Whittier Narrows earthquake. (a) Map view of maximum stress change for depth range of 10.0–14.4 km, with seismicity (1 October 1987 to 31 December 1994, $M \geq 1.0$, horizontal error <0.5 km) from *Shearer* [1997] for the same depth range. The source fault model, shown by the black inscribed line, has tapered thrust slip on a 4.5 × 4.5 km fault with strike 270°, dip 25°, and rake 90°, following *Lin and Stein* [1989]; receiver faults are assumed to have the same parameters. (b) Coulomb stress change in cross section cutting the center of the fault. The resulting stress component is shown in the top left-hand corner. (c) Normal stress change. Unclamping is positive. There were no earthquakes recorded during 1975–1987 at the minimum catalog magnitude of $M \geq 0.8$ [*Richards-Dinger and Shearer*, 2000], and so the aftershock pattern is more likely a response to the stress changes imparted by the main shock than a continuation of the background seismicity.

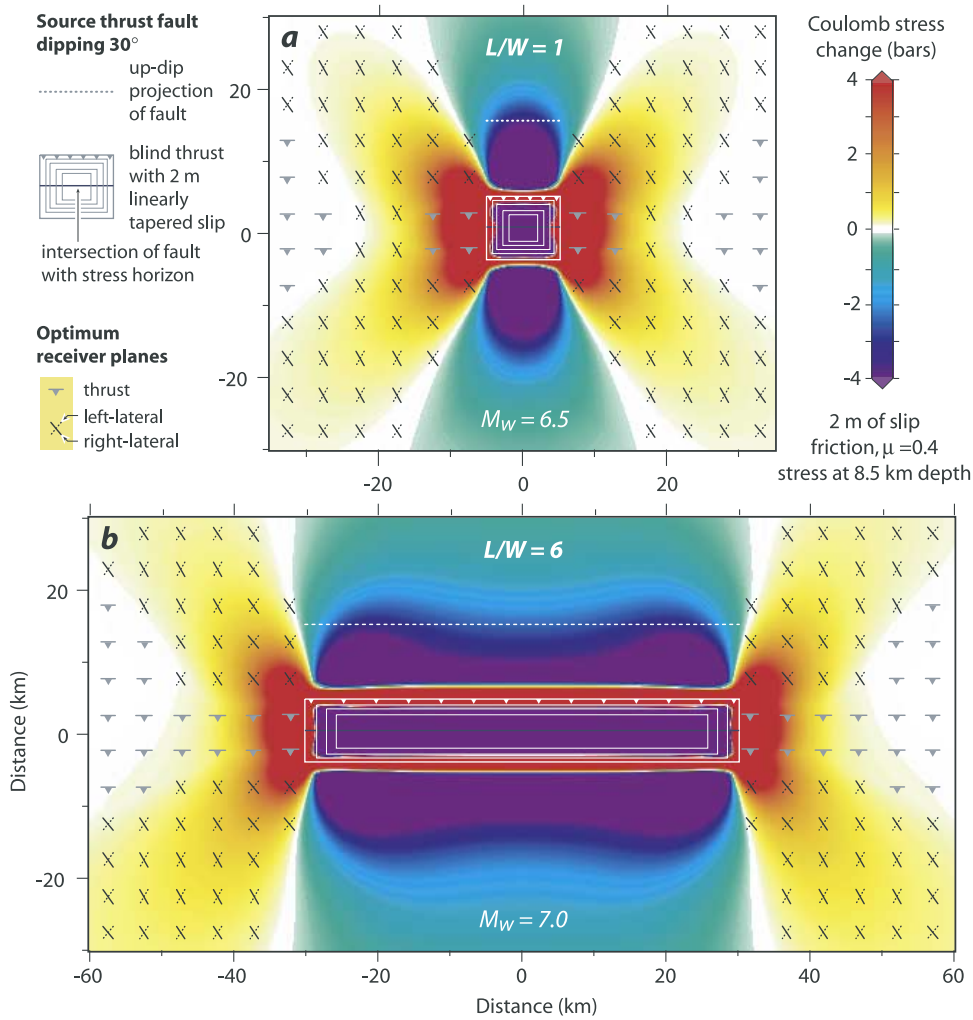

Figure 4. Stress transferred by (a) short versus (b) long blind thrust source faults dipping 30°. Stress is sampled on a horizontal plane bisecting the fault. To illustrate which type of receiver fault is most likely to be promoted, stress is calculated on optimally oriented receiver faults; in other words, at every point the plane on which the Coulombs stress change is most positive is shown. The stress increases beyond the ends of the long and short source fault are about the same, but the zone of stress decrease perpendicular to the strike of the source fault is much broader along strike for the long fault. While thrust faulting is promoted beyond the ends of a thrust fault rupture, the region over which strike-slip faulting is enhanced extends over a much larger area.

ruptures are efficient in inhibiting thrust faults in a large region perpendicular to the rupture plane.

3. Stress Transfer in a Continental Blind Thrust Sequence

[13] The central California Coast Ranges suffered a southeast propagating sequence of blind thrust earthquakes that includes the 1982 M_w = 5.8 New Idria, 1983 M_w = 6.7 Coalinga, 1983 M_w = 6.0 Nuñez, and 1985 M_w = 6.0 Kettleman Hills earthquakes. The main shocks were separated by 8, 2, and 25 months, respectively. In keeping with most studies, we treat the events as occurring on west dipping thrust faults, although it should be noted that *Dickinson* [2002] argues that the shocks most likely struck on east dipping reverse faults. Although stress transferred by the New Idria to the Coalinga shock is negligible (Figure 7a), the stress imparted by the Coalinga event to the Nuñez rupture plane is large (Figure 8), suggesting that the Coalinga shock promoted the Nuñez earthquake. The Coulomb stress increase at the base of the Nuñez fault is about 4–10 bars (Figures 8a and 8b), and is unclamped by 20 bars, because of its proximity to the Coalinga source (Figure 8d).

[14] Aftershocks of the New Idria and Coalinga events are concentrated in regions of calculated Coulomb stress increase (Figures 7a and 7b), although this is less true for the Kettleman Hills aftershocks (Figure 7c). In cross section, the distributed pattern of Coalinga aftershocks in the epicentral area (Figure 9b) and at the future epicenter of the Kettleman Hills shock (Figure 9c) is also in rough accord with the calculated Coulomb stress change. The absence of such correlations between background seismicity and the subsequent earthquake stress changes (Figures 7d–7f and Figures 9d–9f) furnishes additional support that after-

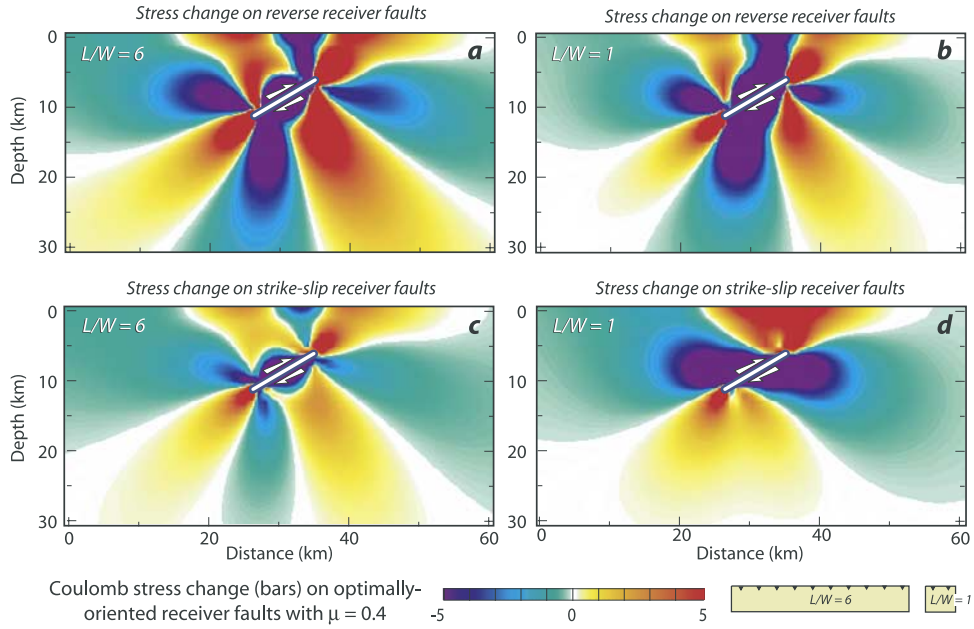

Figure 5. Cross-sectional areas across the midpoint of a thrust fault, showing stresses imparted by a 30°-dipping blind thrust source fault on nearby (a, b) reverse and (c, d) strike-slip receiver faults. The pattern of stress change on strike-slip receiver faults differs markedly for long (Figure 5c) and short (Figure 5d) source faults. Strike-slip faulting is also enhanced above a blind thrust fault (Figure 5d). These cross sections can be compared with the map view for the same cases in Figure 4.

shocks are the product of the coseismic stress changes, rather than being a continuation of the background seismicity.

4. Stress Transfer in Subduction Events

[15] The most robust features of subduction seismicity are the occurrence of thrust aftershocks on the periphery of the seismic rupture and along its downdip extension, and the occurrence of normal faulting aftershocks in the outer rise, seaward of the trench (Figure 10a). Normal faulting events are abundant in the outer rise during the decades after the main shock, whereas thrust events in the outer rise are only seen in the decades before the next main shock (Figure 10b) [*Lay et al.*, 1989]. To explain these observations, we first investigate the stresses transferred by a great subduction earthquake to surrounding faults, and then examine the distribution of stress on the rupture surface for two well-determined earthquakes.

[16] To interpret the aftershock patterns seen in subduction zones, we calculate the stress that large main shocks impart to the surrounding crust. Normal faulting is promoted in the upper lithosphere and inhibited downdip of the rupture in the Wadati-Benioff zone (Figure 11a). In contrast, thrust faulting is promoted in the Wadati-Benioff zone, but is inhibited in the upper lithosphere except in a narrow region in the back arc, above the lower edge of the source fault (Figure 11b). The outer rise is the product of tensional stresses caused by the bending of the oceanic lithosphere [*Hanks*, 1971], whereas thrust earthquakes accommodating subduction delineate the Wadati-Benioff zone [*Ruff and Tichelaar*, 1996]. The net effect of these stress changes is therefore to promote normal-faulting events in the outer rise and thrust events in the Wadati-Benioff zone (Figure 11c); in some cases, the subduction event also triggers thrusting in the back arc. Static stress transfer can thus explain the classic results of *Lay et al.* [1989], including the increase in outer rise normal faulting following major subduction earthquakes (Figure 10b). Using a two-dimensional viscoelastic model, *Taylor et al.* [1996] first reached similar conclusions for the outer rise interactions, and we confirm their interpretation. *Taylor et al.* [1998] used a three-dimensional elastic model to investigate strike-slip faulting in the back arc triggered by subduction events.

5. Aftershock Triggering by Great Subduction Earthquakes

[17] Close inspection of earthquake triggering in subduction zones requires detailed models of the distribution of coseismic slip. *Barrientos and Ward* [1990] developed a variable slip model for the world's largest recorded earthquake, the 1960 $M_w = 9.5$ Chile event, by inverting geodetic and coastal uplift observations. We used their slip model to calculate the Coulomb stress changes on the rupture plane and in its immediate vicinity (Figure 12a). The model reveals large stress concentrations on and off the fault. When resolved on the rupture plane, 75% of the aftershocks occur where the stress change is positive (Figure 12a). Two $M \geq 7$ shocks that struck in 1974–1975 also lie in regions of calculated stress increase. The few well-located aftershocks that lie beneath the rupture plane also occur in where the stress increased (Figure 12b). Aftershocks extend farther from the north end of the rupture zone than they do from the south end, an observation also consistent with the off-fault stress increases.

[18] Although considerably smaller, aftershocks of the 1995 $M_w = 8.1$ Antofagasta, Chile, earthquake are much better located, permitting a stronger test of stress triggering.

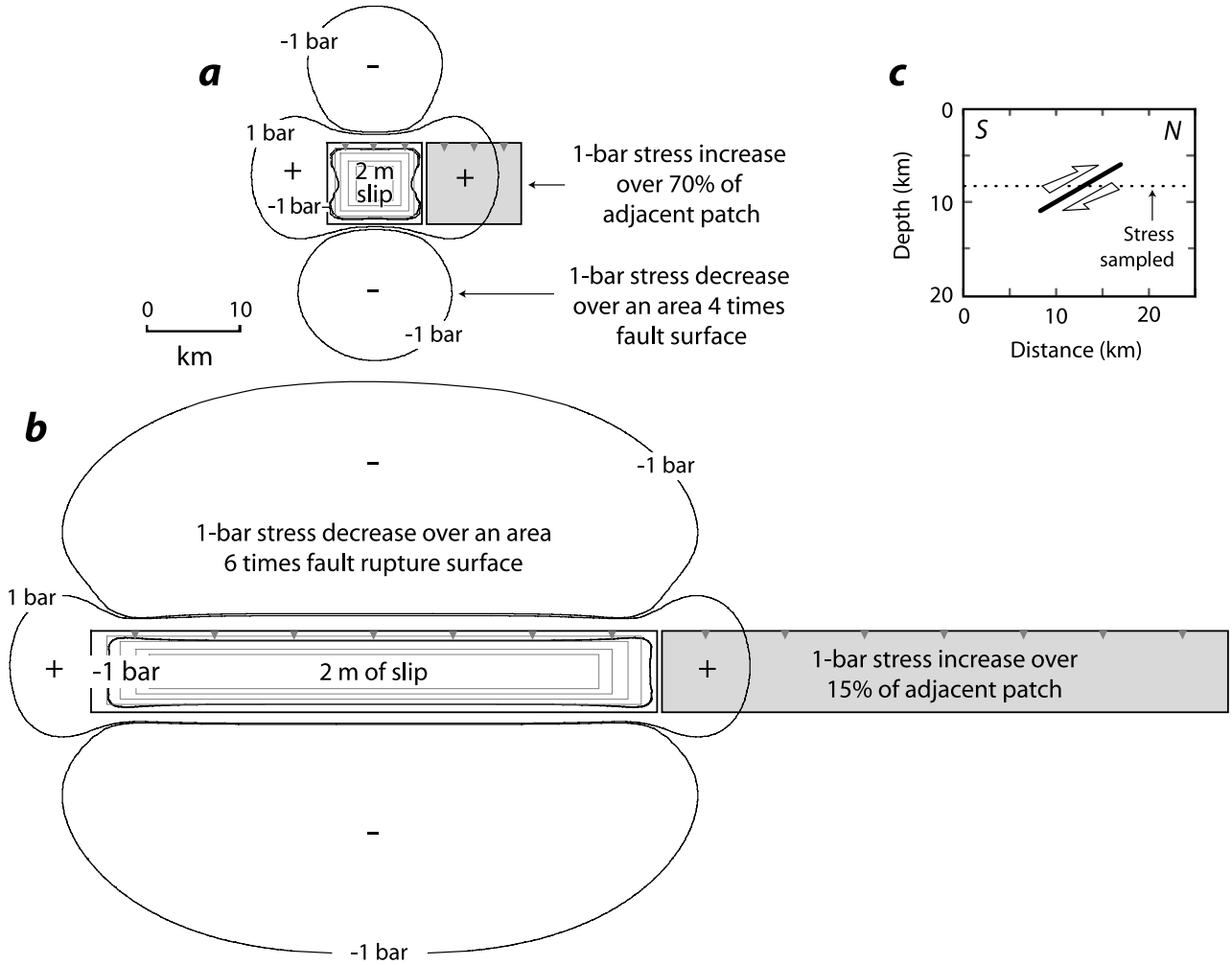

Figure 6. Triggering of a thrust earthquake on an adjacent patch (shaded) of similar size along strike. The source and receiver faults both dip 30°; 2 m of linearly tapered slip, as indicated by the nested rectangles, is imposed on both the short and long source faults. (a) For a square source (L/W = 1), equivalent to M_w = 6.5 with a mean stress drop of 60 bars. A 1-bar stress increase occurs over 70% of the adjacent patch. (b) For a long source (L/W = 6), equivalent to M_w = 7.0 with a mean stress strop of 47 bars. Only 15% of the adjacent patch experiences a 1-bar stress increase. In both Figures 6a and 6b, the downdip width, W, of the source fault controls the along-strike extent of the 1-bar stress increase area in the adjacent fault patch. (c) Cross section showing fault geometry.

Klotz et al. [1999] inverted GPS data for a variable slip model for the 1995 shock, M. Chlieh et al. (Crustal deformation and fault slip during the seismic cycle in the north Chile subduction zone, from GPS and InSAR observations, submitted to *Geophysical Journal International,* 2003, hereinafter referred to as Chlieh et al., submitted manuscript, 2003) inverted GPS and InSAR geodetic data for the first 3 years of postseismic slip, and *Husen et al.* [2000] relocated 1995 aftershocks using local earthquake tomography from a 90-day land and ocean bottom seismometer deployment. We calculate the coseismic Coulomb stress change on the fault surface, and compare this to the principal aftershocks and site of postseismic slip (Figure 12c). Four out of the six largest shocks (red stars), and 82% of the well-relocated aftershocks (circles) lie in areas brought closer to Coulomb failure by the coseismic slip. Aftershocks extend farthest from the north end of the rupture, where the off-fault stress changes are greatest. In addition, the postseismic slip lies on the downward portion of the subduction interface at a locality where the Coulomb stress was most increased by the coseismic slip (Figure 12c). In cross section, some 80% of the aftershocks are located in areas of increased Coulomb stresses, especially downdip of the fault zone (Figure 12d). For neither the 1960 nor the 1995 events is the background seismicity well enough located to permit a comparison of pre-main shock and post-main shock seismicity, as we did for the California thrust faults.

6. Stress Transferred by the San Andreas to Nearby Thrust and Strike-Slip Faults

[19] The stress changes caused by a strike-slip earthquake are most commonly calculated for strike-slip receiver faults

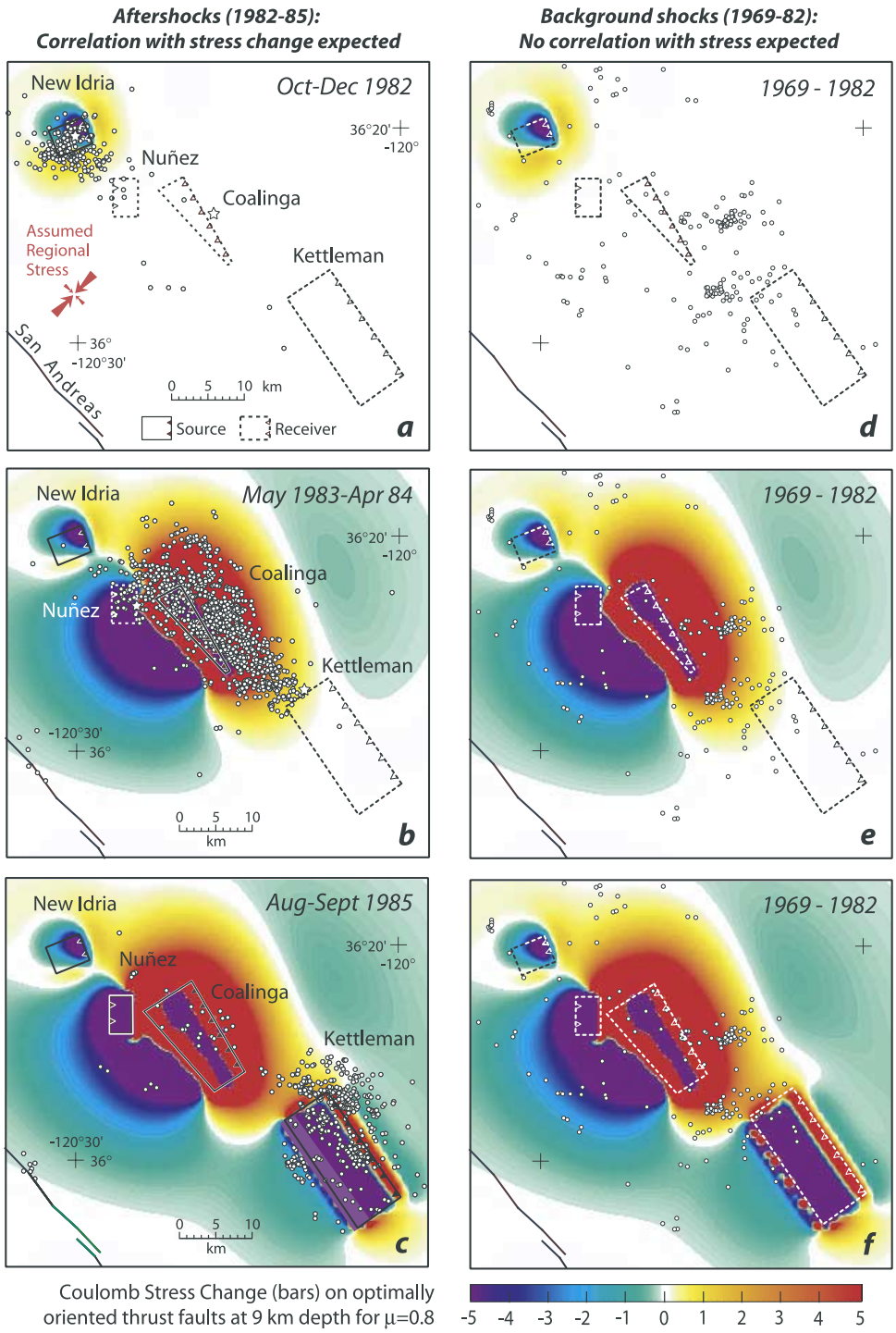

Figure 7. The 1982–1985 Coalinga earthquake sequence; receiver faults are optimally oriented for the regional stress shown in Figure 7a. (a) The 25 October 1982 M_w = 5.8 New Idria earthquake stress changes and aftershocks (25 October 1982 to 31 December 1982, $M \geq 1.0$). (b) Stress from the New Idria and 2 May 1983 M_w = 6.7 Coalinga earthquake, with aftershocks of the Coalinga and Nuñez events (2 May 1983 to 24 April 1984, $M \geq 2.0$). The Coalinga shock brings both the 22 July 1983 M_w = 6.0 Nuñez and 4 August 1985 M_w = 6.0 Kettleman Hills faults closer to failure. (c) Stress from the New Idria, Coalinga, Nuñez, and Kettleman Hills earthquakes, with aftershocks of the Kettleman Hills event (3 August 1985 to 15 September 1985 $M \geq 0.7$). (d–f) Earthquake stress compared with background seismicity 10–60 km northeast of the San Andreas fault (1 December 1969 to 30 September 1982, horizontal error of <1.5 km, depth of ≤20 km, $M \geq 1.5$) from *Stein and Ekström* [1992]. Aftershocks are correlated with stress changes, whereas background seismicity is not, suggesting a causal relationship.

that are parallel to the main rupture [e.g., *King et al.*, 1994] (Figure 13a). However, if the receiver faults are not parallel to the main rupture or are thrust planes, the resulting stress patterns are quite different (Figures 13b–13d). These cases are idealizations of the pattern of stress transfer from the great 1857 M_w = 7.9 Fort Tejon earthquake to existing nearby thrust and strike-slip faults, including the Coalinga thrust belt (Figure 13b), the White Wolf reverse fault (Figure 13c), and the Garlock strike-slip system (Figure 13d).

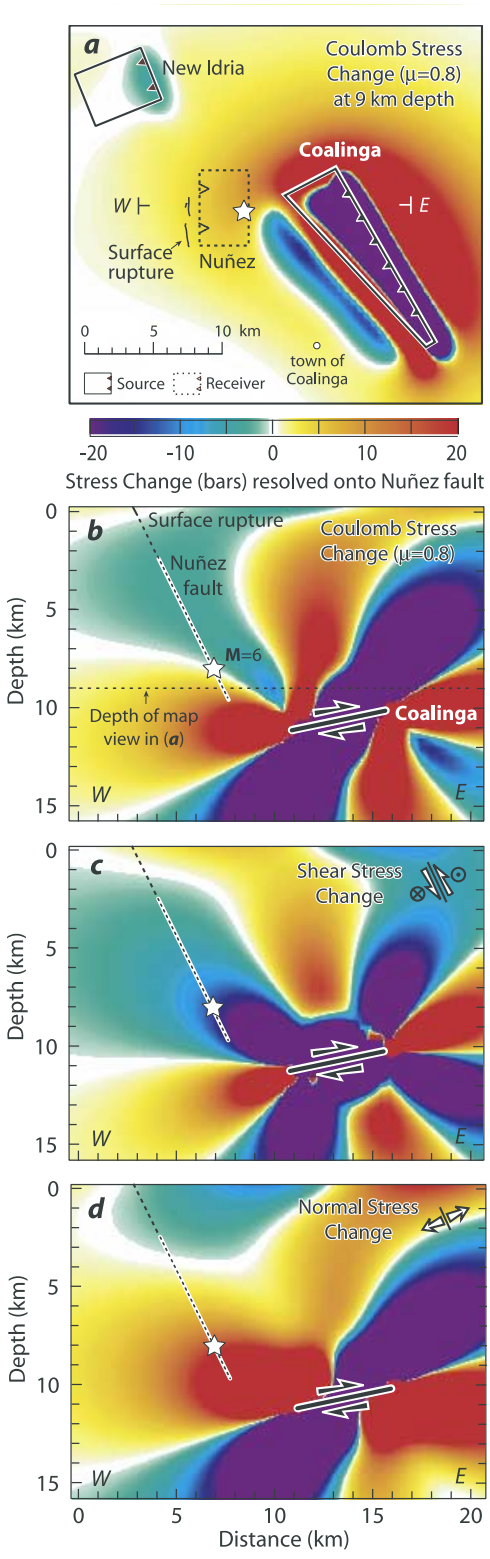

Figure 8. Stress changes caused by the 1982 M_w = 5.8 New Idria and 1983 M_w = 6.7 Coalinga source faults resolved onto the plane of the subsequent 1983 M_w = 6.0 Nuñez rupture (receiver fault, strike 0°, dip 65°, rake 109°). (a) Map view of Coulomb stress changes at 9 km depth. Coalinga parameters are from *Ekström et al.* [1992]; Nuñez parameters are from *Eaton* [1990]. (b) Coulomb stress changes, (c) shear stress changes, and (d) unclamping in cross section resolved on the Nuñez rupture plane. The resultant stress components are shown graphically in the top right-hand corner in Figures 8c–8d). The Nuñez surface rupture was first seen 40 days after the Coalinga main shock, at the time of a shallow M = 5.3 shock on the Nuñez fault; the largest M_w = 6.0 shock occurred 41 days later [*Rymer et al.*, 1990].

6.1. Stress Transferred to the Coalinga Thrust Belt

[20] The 1982–1985 Coalinga sequence slipped only a small portion of a chain of blind thrust faults that runs parallel to the San Andreas fault (Figure 14a). These faults accommodate several mm/yr of shortening perpendicular to the strike of the San Andreas [*Bennett et al.*, 1999]. Why have the thrust faults in only a relatively confined region ruptured during the past century? We calculate that these thrust faults were uniquely stressed both by the 1857 M_w = 7.9 Fort Tejon earthquake (Figure 14b), and by the succeeding 125 years of interseismic stress accumulation (Figure 14c). The New Idria and Coalinga faults were brought ~0.25 bars closer to Coulomb failure by the 1857 earthquake (Figure 15a); this pattern can be compared to the simpler case shown in Figure 13b. We note that a 12 April 1885 M_w ~6.5 earthquake struck somewhere near Coalinga 28 years after the Fort Tejon event [*Toppozada et al.*, 1981]. The intensity V isoseismal for the 1885 shock is located 5–25 km north of the 1983 Coalinga event [*Stein and Ekström*, 1992], and so a thrust earthquake may have occurred in the region brought closest to failure by the 1857 event.

[21] Because the San Andreas creeps northwest of Parkfield (Figure 14c), interseismic stress that promotes thrust faulting continuously builds east of Parkfield in the vicinity of the Coalinga and Kettleman Hills ruptures (Figure 15b). During the 125 years after 1857, we calculate that the stress increased by 1.5 bars at Coalinga, but became strongly negative to the southeast (Figure 15b). We note that our interseismic stress accumulation is likely oversimplified, and could be an underestimate if postseismic stressing were accelerated by viscoelastic relaxation [*Pollitz and Sacks*, 1992].

[22] The addition of the seismic and interseismic stress thus favors thrust faulting near Coalinga (Figure 15c). In contrast, at the average Holocene San Andreas slipping rate, the long-term stress transferred to the thrust belt by the San Andreas in one average earthquake cycle shows no stress concentration near Coalinga (Figure 15d). This is because the long-term stresses are principally caused by the fault bend, whereas the short-term concentration in stress is collectively caused by the bend, the 1857 slip distribution,

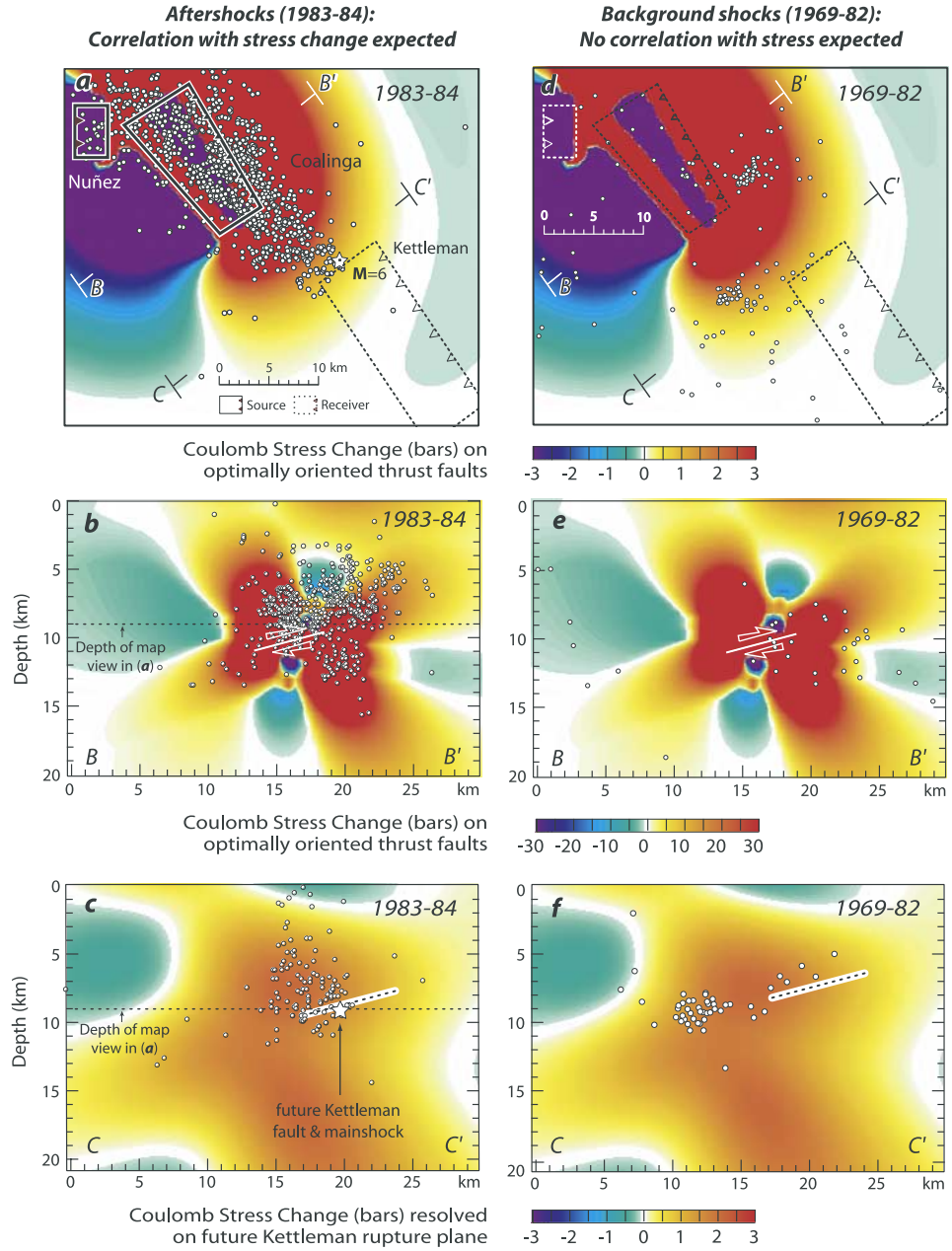

Figure 9. Stress changes caused by the 1983 M_w = 6.7 Coalinga and M_w = 6.0 Nuñez ruptures. The Coalinga source includes postseismic slip that occurred before the 1985 M_w = 6.0 Kettleman Hills rupture. (a) Map view at 9 km depth with Coalinga aftershocks (2 May 1983 to 4 April 1984, $M \geq 2.0$), showing a correspondence with stress changes, including a 1-bar stress increase at the future Kettleman Hills epicenter. (b) Coulomb stress changes along profile B-B′, together with aftershocks along an 8-km-wide band. Note stress scale difference. (c) Coulomb stress changes along profile C-C′ within 5 km of the future Kettleman Hills epicenter, together with aftershocks along an 8-km-wide band. Stress is imparted by the Coalinga earthquake, resolved onto the future Kettleman Hills rupture plane (strike 142°, dip 12°, rake 109°, from *Ekström et al.* [1992]). (d–f) Background seismicity (1 December 1969 to 30 September 1982), as in Figure 7, showing no such correlations with the future coseismic stress changes.

and the absence of a full cycle of interseismic stress accumulation during 1857–1983.

6.2. Stress Transferred to the White Wolf Thrust Fault

[23] The 1952 M_w = 7.3 Kern County shock, which ruptured the White Wolf reverse fault at the southern end of the Coast Ranges fold belt (Figure 14a), also appears to have been promoted by the 1857 earthquake, as previously reported by *Harris and Simpson* [1996] and *Deng and Sykes* [1997]. We calculate that the 1857 earthquake increased the stress at the epicentral end of the White Wolf fault by 8 bars (Figure 16a). This pattern can be

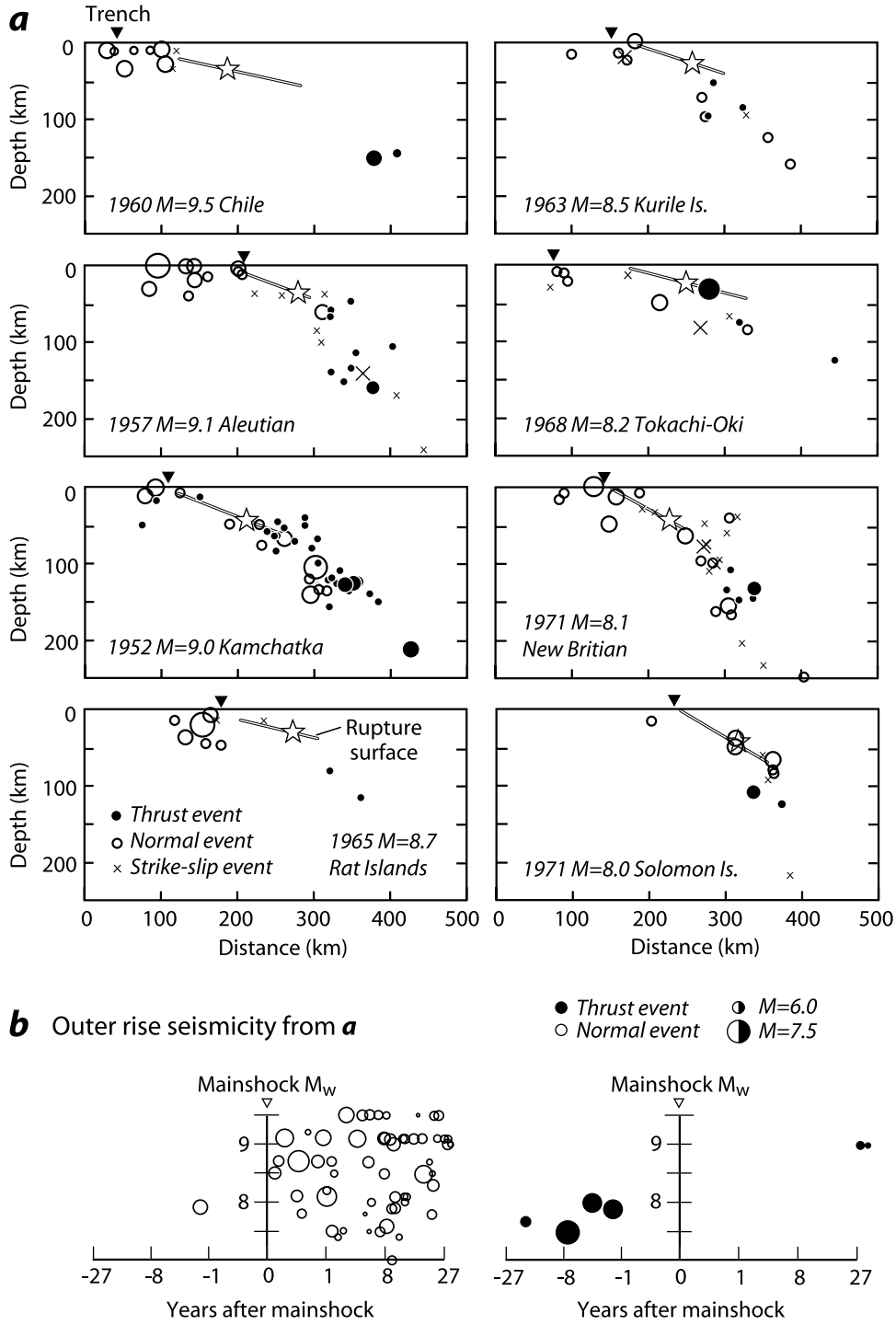

Figure 10. Subduction seismicity. (a) Cross sections through subduction rupture zones [from *Lay et al.*, 1989]. The approximate rupture surface, hypocenter (star), and aftershocks are shown, along with the position of the trench. Aftershock magnitude is proportional to symbol size. Earthquake legend is in the bottom left-hand panel. Oceanward of the trench, the normal events are dominant; thrust events are more common on the downdip portion of the subduction interface. (b) Changes in outer rise seismicity following great subduction earthquakes from *Lay et al.* [1989], based on the data of *Christensen and Ruff* [1988]. Normal-faulting events become abundant after subduction earthquakes (left); thrust events become less common after the main shock (right). In Figure 10b, seismicity is located on the vertical axis at the magnitude of the associated main shock. Circle size is proportional to the magnitude of the aftershock or pre-main shock event, and the timescale is nonlinear. For example, outer rise tensional aftershocks of the 22 May 1960 $M_w = 9.5$ Chile event are evident 2–27 years after the main shock with $4 \leq M \leq 7$ (left); no outer rise thrust events are seen before or after the 1960 Chile shock (right).

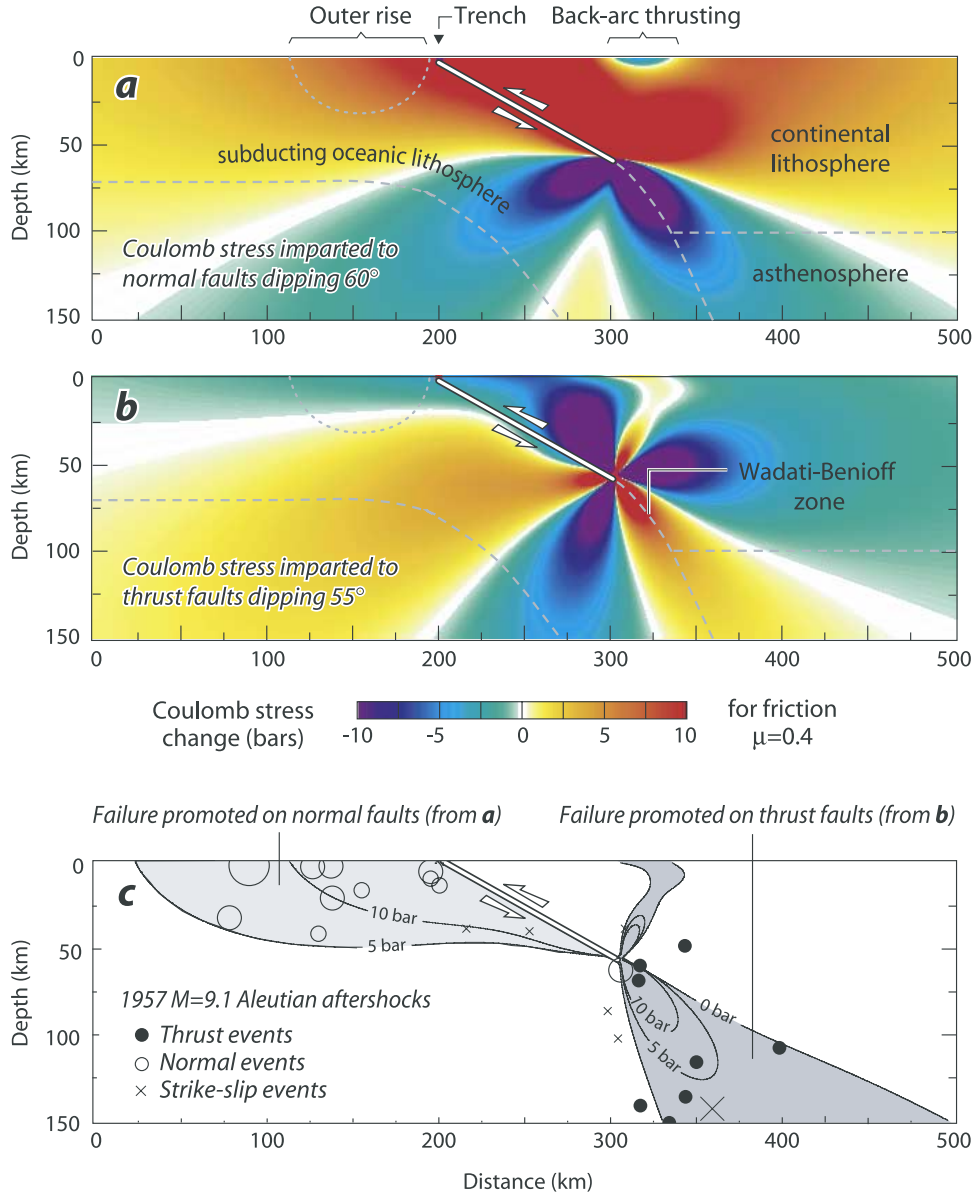

Figure 11. Stress change and seismicity associated with a great subduction earthquake. (a) Coulomb stress imparted to normal receiver faults, with plate tectonic features labeled. Note stress increase in the outer rise, where normal faults are abundant. (b) Coulomb stress imparted to thrust receiver faults dipping 55°, which reflects the overall subduction slab dip beneath the rupture plane of the 1957 M_w = 9.1 Aleutian earthquake. Note stress increase on the downdip portion of the subduction interface. (c) Composite showing stress imparted to existing faults. Because of permanent tension in the outer rise caused by bending, normal faults predominate in the upper 35 km seaward of the trench. Because of subduction, thrust faults predominate in Wadati-Benioff Zone. Where normal faults are dominant, stresses from Figure 11a are shown; where thrust faults are dominant, stresses from Figure 11b are shown. The stresses are superimposed on aftershocks of the 9 March 1957 M_w = 9.1 Aleutian earthquake ($M_0 = 5 \times 10^{29}$ dyn cm, dip 28°), showing a good correspondence with the model.

compared with the idealization in Figure 13c, although the latter lacks the big bend that further concentrates stress at the White Wolf location (Figure 16a). The White Wolf fault is also optimally positioned to be stressed by long-term San Andreas slip (Figure 16b); we calculate that stress grows on the White Wolf fault at a rate of 1.5 bars per century due to long-term San Andreas slip. The interevent time of large earthquakes on the White Wolf fault is about 1000–2000 years [*Stein and Thatcher*, 1981], and so San Andreas slip brings the White Wolf fault 15–30 bars closer to failure every White Wolf earthquake cycle, which is about equal to the earthquake stress drop for the White Wolf event. The particular slip distribution in 1857 added another 8 bars or 25–50% to

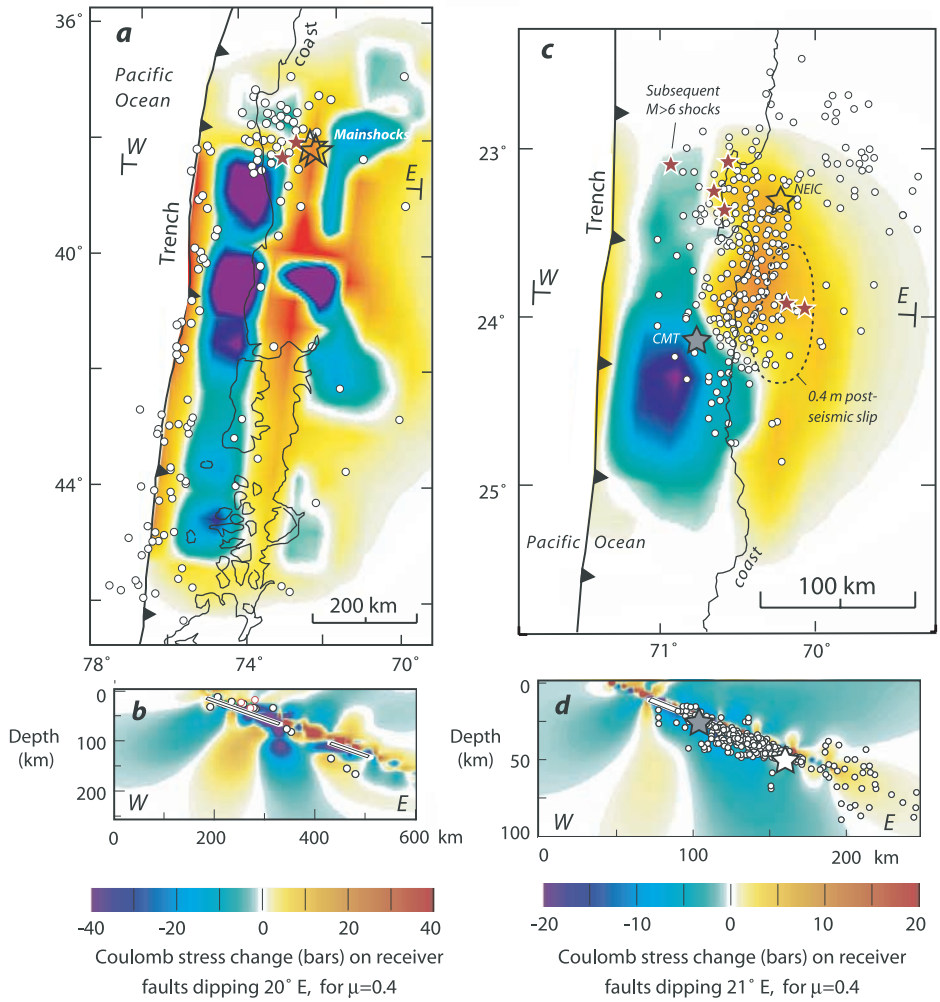

Figure 12. Calculated stress changes for two great Chilean subduction earthquakes. (a) Coulomb stress changes associated with the 22 May 1960 M_w = 9.5 Chile earthquake, using the variable slip planar model of *Barrientos and Ward* [1990], which assumes a uniform rake equal to the plate convergence vector on a 20°-dipping plane, smoothed to 50 × 50 km patches. Stress changes are superimposed on aftershocks from *Cifuentes* [1989] (International Seismological Centre and International Seismological Service catalogs, 21 May 1961 to 31 December 1983, $M \geq 5.8$). Small red stars are 18 August 1974 M_s = 7.1 and 10 May 1975 M_s = 7.8 shocks, and large black stars are the main 1960 subevents. About 75% of the aftershocks lie in regions of calculated Coulomb stress increase. Stress is calculated on dipping planes encompassing the rupture surface and projected onto ground surface. Because this calculation is on the rupture surface, shear stress changes dominate. (b) Cross section of stress changes along W-E in (a), with corresponding aftershocks along the profile from *Cifuentes* [1989] (red circles) and *Kadinsky-Cade* [1985] (black circles). (c) Coulomb stress changes associated with the 30 July 1995 M_w = 8.1 Antofagasta, Chile, earthquake, based on the variable slip model of *Klotz et al.* [1999], smoothed to 25 × 25 km patches (the model of *Ihmlé and Ruegg* [1997] yielded similar patterns of stress changes with minor differences in detail). Large white and gray stars show the NEIC epicenter and the Harvard centroid moment tensor (CMT), respectively, while small circles show 1995 aftershocks located by tomographic inversion by *Husen et al.* [2000] from a 90-day seismometer deployment. $M_w \geq 6.0$ aftershocks during the first 3.3 years following the main shock are shown as red stars. The site of postseismic slip inferred from geodetic observations by Chlieh et al. (submitted manuscript, 2003) is shown as the dotted contour. Stress is calculated on dipping planes encompassing the rupture surface and projected onto ground surface. (d) Cross section of stress changes with 1995 aftershocks from *Husen et al.* [2000].

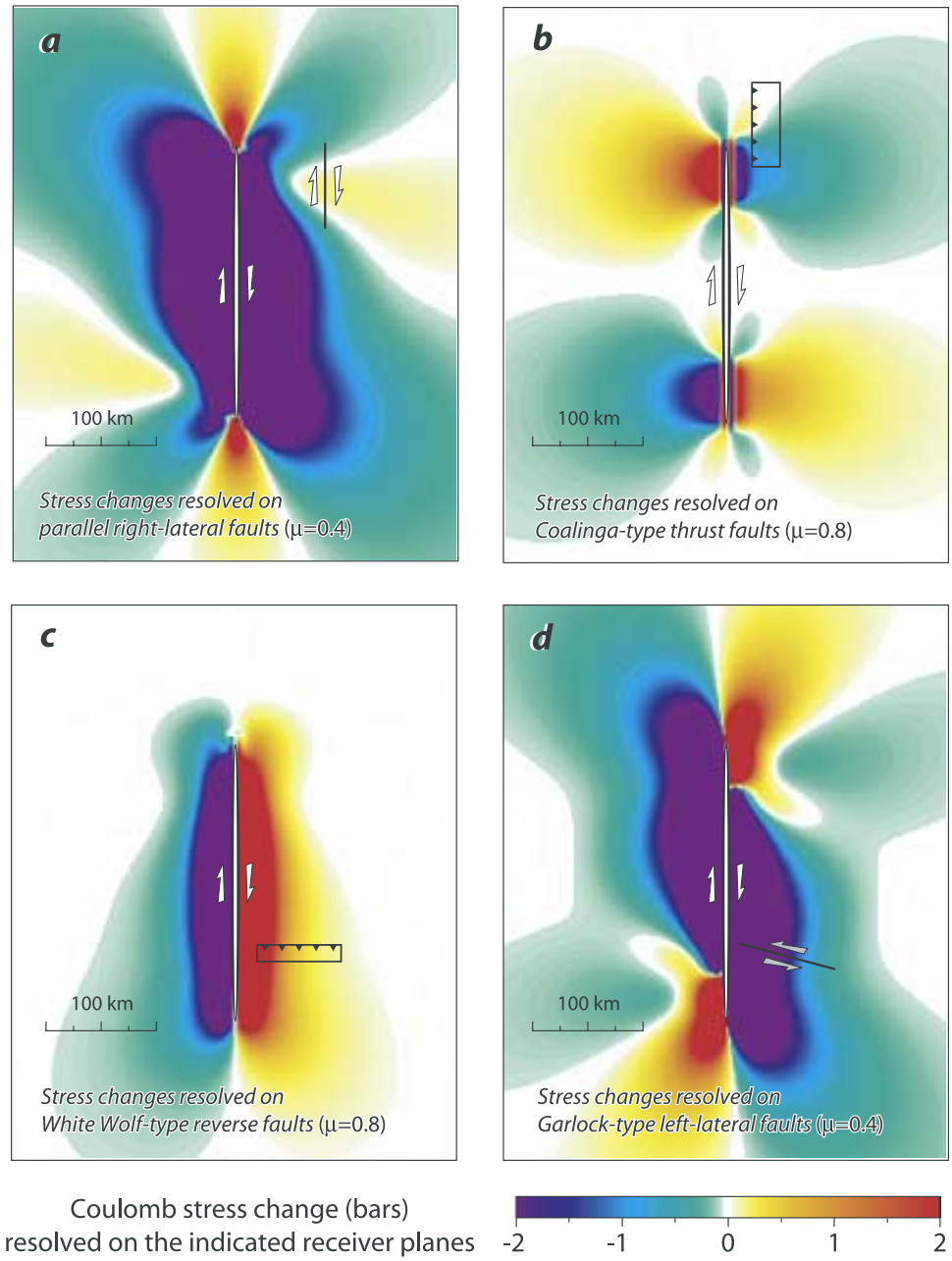

Figure 13. Schematic M_w = 7.9 rupture on a vertical right-lateral fault to illustrate stress transferred to receiver faults of various geometries and rakes. The rupture is 250 km long and 15 km deep, with 7.5 m of uniform slip extending over the central 150 km, tapering linearly to zero 50 km from each end; M_0 = 7.2×10^{27} dyn cm. Stress is sampled at 7.5 km depth. In Figures 13a–13d, examples of such a receiver fault are shown at one location, but the stress changes are plotted for such receiver faults at all locations. The main rupture resembles that of the 1857 M_w = 7.9 Fort Tejon earthquake except for the lack of the San Andreas big bend and variable 1857 slip. Calculated stress changes (a) for right-lateral receiver planes parallel to the main rupture (strike 0°, dip 90°, rake 180°) [e.g., *King et al.*, 1994]; (b) for thrust receiver faults parallel to the source quake (strike 0°, dip 20°, rake 90°), as an idealized representation for the Coalinga thrust belt; (c) for thrust receiver faults perpendicular to the main rupture (strike 90°, dip 45°, rake 90°), as an idealized representation for the White Wolf reverse fault; and (d) for left-lateral receiver faults (strike 109°, dip 90°, rake 0°), as an idealized representation for the Garlock strike-slip system. We use μ = 0.4 in Figures 13a and 13d for strike-slip receiver faults with significant cumulative slip and μ = 0.8 in Figures 13b and 13c for thrust faults that may be sensitive to changes in normal stress.

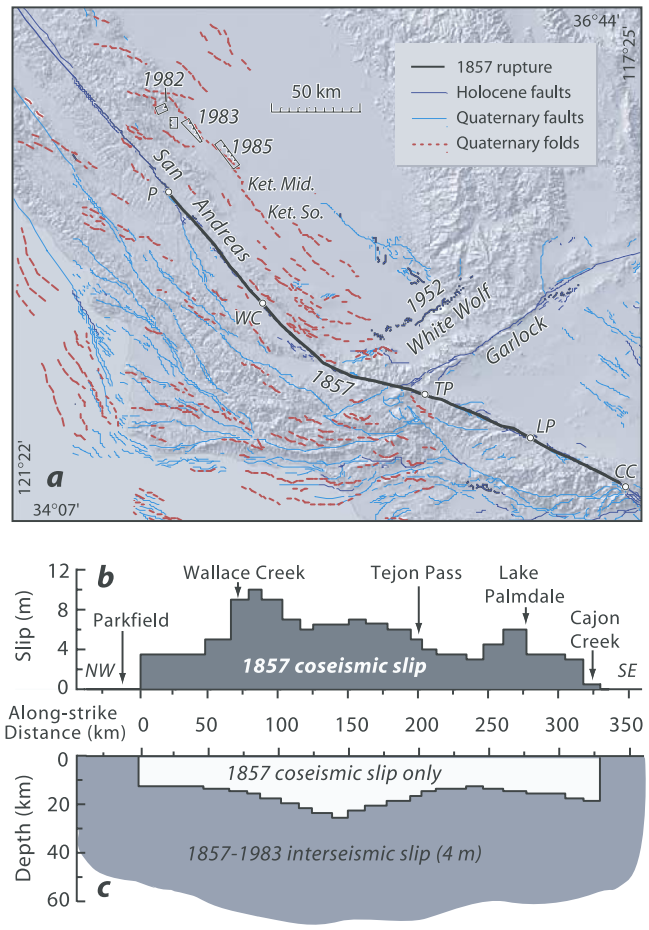

Figure 14. Southern California fault system and San Andreas slip model. (a) Active faults and folds with earthquake sources shown by their dates. Quaternary folds are surrogates for blind thrust faults [*Stein and Yeats*, 1989; *Lettis et al.*, 1997] (P, Parkfield; WC, Wallace Creek; TP, Tejon Pass; LP, Lake Palmdale; CC, Cajon Creek; Ket. Mid., Kettleman Middle Dome; Ket. So., Kettleman South Dome). Blind thrust faults extend parallel to the San Andreas fault nearly as far south as the White Wolf reverse fault. (b) The 9 January 1857 Fort Tejon M_w = 7.9 earthquake slip model from *Sieh* [1978], as modified by subsequent work [*Weldon and Sieh*, 1985; *Salyards et al.*, 1992; *Grant and Sieh*, 1993; *Grant and Donnellan*, 1994]. (c) Interseismic stressing model for the period between the 1857 Fort Tejon and 1983 Coalinga events, in which the San Andreas fault slips at the long-term rate everywhere except in the 1857 rupture zone. The assumed depth of 1857 faulting is based on the current lower depth of seismicity from *Hill et al.* [1990], as shown in Figure 14c. Slip in Figures 14b and 14c is right lateral.

this amount, perhaps hastening the occurrence of the Kern County earthquake.

6.3. Stress Transferred to the Garlock Strike-Slip Fault

[24] If San Andreas slip indeed promoted failure on the White Wolf thrust fault, why has the Garlock fault, just 30 km to the south, also not ruptured since 1857? We find that the 1857 Fort Tejon earthquake and long-term San Andreas stressing yield a very different fate for the left-lateral Garlock fault than for the White Wolf thrust system. The 1857 earthquake inhibited failure on the left-lateral Garlock fault by 1–4 bars (Figure 16c; the idealized case is shown in Figure 13d), while long-term slip on the San Andreas promotes failure only on the central Garlock fault by a modest ~0.3 bars/century (Figure 16d). The stress decrease associated with the 1857 event may explain why the current strain accumulation rate on the central Garlock fault measured by GPS and trilateration is near zero [*Miller et al.*, 2001; *Savage et al.*, 2001], despite a Holocene slip of 5–7 mm/yr [*McGill and Sieh*, 1993]: The 1857 earthquake may have retarded the accumulation of stress on the Garlock fault during the past 150 years (Figure 16c). Two prehistorical events are documented on the Garlock fault during the preceding 400 years, the last of which ruptured sometime during 1490–1810 [*McGill and Rockwell*, 1998; *Dawson et al.*, 2003]. The Garlock slip rate may itself be controlled by the left-lateral stress imparted by the long-term San Andreas slip, since they are both highest along the central Garlock fault (Figure 16d). No paleoseismic evidence for large earthquakes on the westernmost Garlock has yet been found.

7. Conclusions

[25] Many of the outstanding observations of thrust seismicity are readily explained by the static Coulomb stress changes. These include the tendency of moderate-sized thrust events to progress along strike, distributed aftershock zones and abundant secondary faulting associated with blind thrust ruptures, the prevalence of outer rise normal faulting events following subduction earthquakes, and aftershocks that ring the site of subduction slip. We used published source models and aftershock catalogs for a half dozen thrust earthquakes to calculate the Coulomb stress imparted to the surrounding crust. We calculated that thrust seismicity is promoted by stress increases of 1–25 bars, and is inhibited by stress decreases of the same amount. The stress changes imparted by thrust faults are typically higher than that for normal and strike-slip faults, an attribute seen from the smallest (M_w = 6.0 Whittier Narrows) to largest (M_w = 9.5 Chile) events examined.

[26] In addition to providing further support for the Coulomb hypothesis, the calculations have implications for the seismic behavior of these faults in the future. In particular, we regard it as unlikely that the 1982–1985 Coalinga thrust sequence will progress farther south to Kettleman Middle or South Dome (Figure 14a) because the accumulated stress there since 1857 is calculated to inhibit such thrust faulting (Figure 15). Similarly, despite its Holocene slip rate of 5–7 mm/yr, large earthquakes on the Garlock fault were inhibited by the 1857 Fort Tejon event and so are unlikely to occur until another large San Andreas earthquake redistributes the stress on the Garlock. In Chile, both the 1960 and 1995 subduction events increased the Coulomb stress north of the rupture more than to the south (Figure 12), and so subsequent events are less likely to occur to the south.

[27] Whereas numerous authors have suggested that aftershocks of subduction earthquakes cluster around the periphery of the coseismic slip, we have offered a rigorous

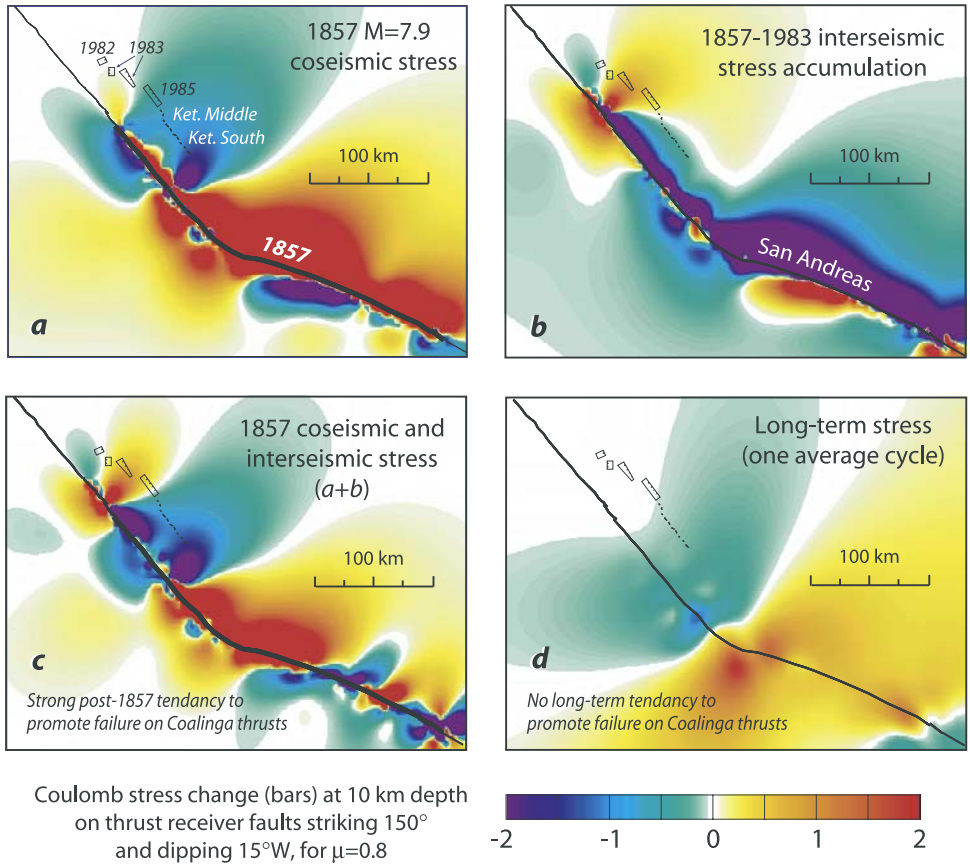

Figure 15. Stress imparted to the Coalinga thrust belt by the San Andreas fault. (a) Coseismic stress transferred by the 1857 M_w = 7.9 Fort Tejon earthquake, resolved onto the Coalinga rupture plane (strike 150°, dip 15°, rake 90°), using the model shown in Figure 14b. The New Idria and Coalinga thrusts are brought closer to failure, whereas the thrust belt immediately to the southeast (Ket. Middle and Ket. South) is inhibited from failure. (b) Interseismic stress accumulation during 1857–1983 using the model shown in Figure 14c. (c) Net stress transferred since 1857, by addition of Figures 15a and 15b. Note concentration of stress in the Coalinga-Kettleman region and a marked decrease to the southeast. (d) No increase in stress near Coalinga in the calculated long-term stress transferred to the thrust belt by the San Andreas in one average earthquake cycle, assuming Holocene average slipping rate on the San Andreas [*Petersen and Wesnousky*, 1994; *Murray et al.*, 2001; *Grant and Lettis*, 2002].

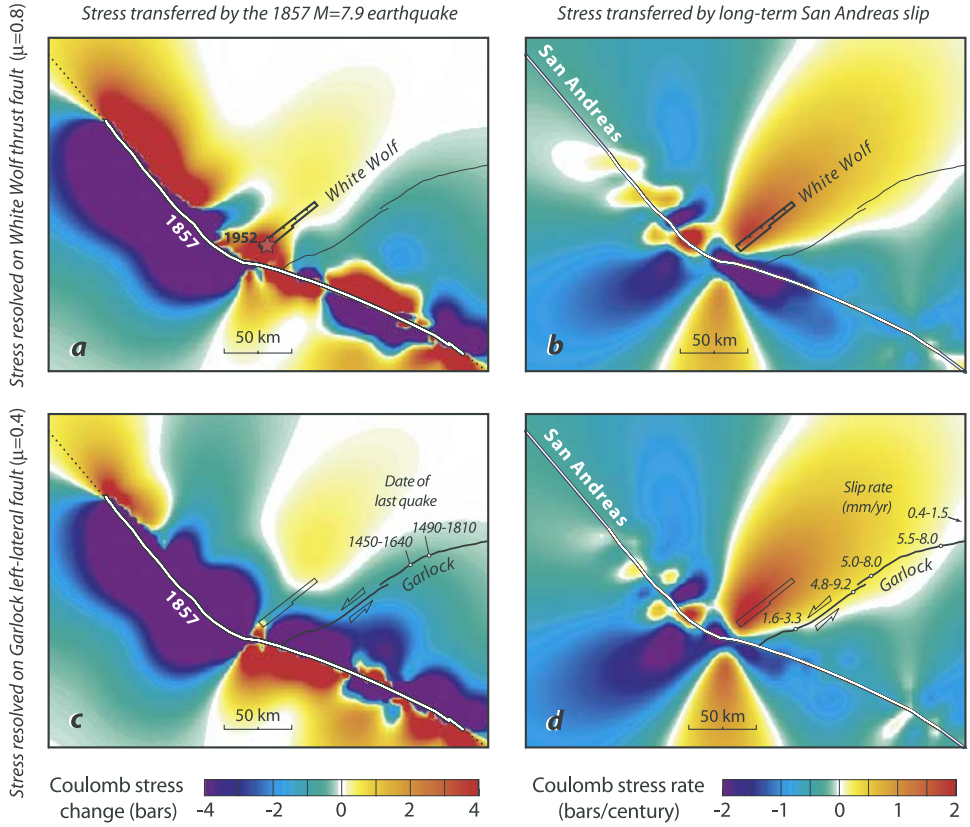

Figure 16. Coulomb stress at a depth of 10 km transferred to the White Wolf thrust and Garlock left-lateral faults by the San Andreas fault. (left) Stress imparted by the 1857 M_w = 7.9 Fort Tejon earthquake; (right) stress due to the long-term San Andreas slip. (a) The 1857 earthquake promoted 8 bars of stress increase at the 20-km hypocentral depth of the 1952 Kern County earthquake. Stress changes are resolved on receiver faults with the 21 July 1952 M_w = 7.3 Kern County earthquake parameters of *Bawden* [2001] for the southwest segment (strike 51°, dip 75°, rake 25°). We use $\mu = 0.8$, since this is a reverse fault with <4 km of cumulative slip. (b) The White Wolf fault calculated to be stressed at a rate of 1.5 bars/century, assuming Holocene average slipping rate on the San Andreas [*Petersen and Wesnousky*, 1994; *Murray et al.*, 2001; *Grant and Lettis*, 2002]. (c) The 1857 earthquake inhibiting failure on the left-lateral Garlock fault by 1–4 bars. Stress changes are resolved on receiver faults with the average Garlock geometry (strike 55°, dip 90°, rake 0°) following *Savage et al.* [2001]. For the Garlock, we use $\mu = 0.4$ because it is strike slip with 64 km of total offset [*Miller et al.*, 2001]; paleoseismic dates are shown [*McGill and Sieh*, 1993; *Dawson et al.*, 2003]. (d) Failure promoted by the long-term San Andreas slip only on the central Garlock, at a modest rate <0.3 bars/century. Perhaps for this reason, the central Garlock fault attains its highest Holocene slip rate [*McGill*, 1998].

exploration of this association for two well-determined events. Aftershocks concentrate where the stress increases by more than about 2 bars, and are all but absent where the stress is calculated to have dropped by more than 10 bars.

[28] Perhaps our most intriguing finding is the proposed interaction between the San Andreas and associated thrust faults. *Harris and Simpson* [1996] argued that the 1857 M_w = 7.9 Fort Tejon earthquake promoted failure of the 1952 Kern County predominantly thrust event by ~2 bars; *Deng and Sykes* [1997] argued that the 1857 event and subsequent interseismic stressing promoted failure of the 1885 M_w ~6.5 shock near Coalinga by ~0.5 bars, the 1952 M_w = 7.3 Kern Country quake by ~10 bars, and the 1983 M_w = 6.7 Coalinga event by ~0.5 bar. We believe that our portrayal of the coseismic, interseismic, and long-term stress transfer makes it easier to understand the nature of these interactions. For the Coalinga thrust, it becomes apparent from Figure 15 that the 1857–1983 interseismic stressing most promotes failure; the 1857 event is far less important. For the White Wolf fault, the opposite is true (Figure 16).

[29] Together with previous investigations, this study furnishes evidence for stress triggering of earthquakes. The phenomenon is apparent on spatial scales of 2–200 km, and timescales of hours to centuries. We therefore believe that building stress transfer into seismic hazard assessment must become a principal objective of earthquake interaction studies.

[30] **Acknowledgments.** We thank Shinji Toda for inspiration, Serkan Bozkurt for technical prowess, and Greg Anderson, Ruth Harris, Michele Cooke, Steven Jaumé, and Cliff Thurber for perceptive reviews. All

calculations were performed using Coulomb 2.5, which can be downloaded with user's guide and tutorial files from http://quake.usgs.gov/~ross. J. L. was supported by the National Science Foundation through grant NSF-EAR0003888; R. S. gratefully acknowledges funding from Swiss Re. Woods Hole Oceanographic Institution contribution 10944.

References

Barrientos, S. E., and S. N. Ward (1990), The 1960 Chile earthquake: Inversion for slip distribution from surface deformation, *Geophys. J. Int.*, *103*, 589–598.

Bawden, G. (2001), Source parameters for the 1952 Kern County earthquake, California: A joint inversion of leveling and triangulation observations, *J. Geophys. Res.*, *106*, 771–785.

Bennett, R. A., J. L. Davis, and B. P. Wernicke (1999), Present-day pattern of Cordilleran deformation in the western United States, *Geology*, *27*, 371–374.

Casarotti, E., and A. Piersanti (2003), Postseismic stress diffusion in Chile and south Peru, *Earth Planet. Sci. Lett.*, *206*, 325–333.

Christensen, D. H., and L. J. Ruff (1988), Seismic coupling and outer rise earthquakes, *J. Geophys. Res.*, *93*, 13,421–13,444.

Cifuentes, I. L. (1989), The 1960 Chilean earthquakes, *J. Geophys. Res.*, *94*, 665–680.

Dawson, T. E., S. F. McGill, and T. K. Rockwell (2003), Irregular recurrence of paleoearthquakes along the central Garlock fault near El Paso Peaks, California, *J. Geophys. Res.*, *108*(B7), 2356, doi:10.1029/2001JB001744.

Deng, J., and L. R. Sykes (1997), Evolution of the stress field in southern California and triggering of moderate-size earthquakes: A 200-year perspective, *J. Geophys. Res.*, *102*, 9859–9886.

Dickinson, W. R. (2002), Reappraisal of hypothetical Franciscan thrust wedging at Coalinga: Implications for tectonic relations along the Great Valley flank of the California Coast Ranges, *Tectonics*, *21*(5), 1039, doi:10.1029/2001TC001315.

Dmowska, R., J. Rice, L. Lovison, and D. Josell (1988), Stress transfer and seismic phenomena in coupled subduction zones during the earthquake cycle, *J. Geophys. Res.*, *93*, 7869–7884.

Eaton, J. P. (1990), The earthquake and its aftershocks from May 2 through September 30, 1983, in *The Coalinga, California, Earthquake of May 2, 1983*, edited by M. J. Rymer and W. L. Ellsworth, *U.S. Geol. Surv. Prof. Pap. 1487*, 113–170.

Ekström, G., R. S. Stein, J. P. Eaton, and D. Eberhart-Phillips (1992), Seismicity and geometry of a 110-km long blind thrust fault, 1, The 1985 Kettleman Hills, California, earthquake, *J. Geophys. Res.*, *97*, 4843–4864.

Freed, A. M., and J. Lin (1998), Time-dependent changes in failure stress following thrust earthquakes, *J. Geophys. Res.*, *103*, 24,393–24,409.

Grant, L. B., and A. Donnellan (1994), 1855 and 1991 surveys of the San Andreas Fault: Implications for fault mechanics, *Bull. Seismol. Soc. Am.*, *84*, 241–246.

Grant, L. B., and W. R. Lettis (2002), Introduction to the special issue on paleoseismology of the San Andreas Fault system, *Bull. Seismol. Soc. Am.*, *92*, 2551–2554.

Grant, L. B., and K. E. Sieh (1993), Stratigraphic evidence for seven meters of dextral slip on the San Andreas fault during the 1857 earthquake in the Carrizo Plain, *Bull. Seismol. Soc. Am.*, *83*, 619–635.

Hanks, T. C. (1971), The Kuril Trench-Hokkaido Rise system: Large shallow earthquakes and simple models of deformation, *Geophys. J. R. Astron. Soc.*, *23*, 173–189.

Hardebeck, J. L., J. J. Nazareth, and E. Hauksson (1998), The static stress change triggering model: Constraints from two southern California aftershocks sequences, *J. Geophys. Res.*, *103*, 24,427–24,437.

Harris, R. A. (1998), Introduction to special section: Stress triggers, stress shadows, and implications for seismic hazard, *J. Geophys. Res.*, *103*, 24,347–24,358.

Harris, R. A., and R. W. Simpson (1996), In the shadow of 1857—The effect of the great Ft. Tejon earthquake on subsequent earthquakes in southern California, *Geophys. Res. Lett.*, *23*, 229–232.

Harris, R. A., R. W. Simpson, and P. A. Reasenberg (1995), Influence of static stress changes on earthquake locations in southern California, *Nature*, *375*, 221–224.

Hauksson, E. (1994), The 1991 Sierra Madre earthquake sequence in southern California: Seismological and tectonic analysis, *Bull. Seismol. Soc. Am.*, *84*, 1058–1074.

Hill, D. P., J. P. Eaton, and L. M. Jones (1990), Seismicity, 1980–1986, in *The San Andreas Fault System, California*, edited by R. E. Wallace, *U.S. Geol. Surv. Prof. Pap.*, *1515*, 115–151.

Husen, S., E. Kissling, and E. R. Flueh (2000), Local earthquake tomography of shallow subduction in north Chile: A combined onshore and offshore study, *J. Geophys. Res.*, *105*, 28,183–28,198.

Ihmle, P. F., and J.-C. Ruegg (1997), Source tomography by simulated annealing using broad-band surface waves and geodetic data: Application to the M_w = 8.1 Chile 1995 event, *Phys. Earth Planet. Inter.*, *131*, 146–158.

Kadinsky-Cade, K. (1985), Seismotectonics of the Chile Margin and the 1977 Caucete earthquake of western Argentina, Ph.D. thesis, Cornell Univ., Ithaca, N. Y.

King, G. C. P., and M. Cocco (2000), Fault interaction by elastic stress changes: New clues from earthquake sequences, *Adv. Geophys.*, *44*, 1–36.

King, G. C. P., R. S. Stein, and J. Lin (1994), Static stress changes and the triggering of earthquakes, *Bull. Seismol. Soc. Am.*, *84*, 935–953.

Klotz, J., et al. (1999), GPS-derived deformation of the central Andes including the 1995 Antofagasta M_w = 8.0 earthquake, *Pure Appl. Geophys.*, *154*, 709–730.

Lay, T., L. Astiz, H. Kanamori, and D. H. Christensen (1989), Temporal variation of large intraplate earthquakes in coupled subduction zones, *Phys. Earth Planet. Inter.*, *54*, 258–312.

Lettis, W. R., D. L. Wells, and J. N. Baldwin (1997), Empirical observations regarding reverse earthquakes, blind thrust faults, and Quaternary deformation: Are blind thrust faults truly blind?, *Bull. Seismol. Soc. Am.*, *87*, 1171–1198.

Lin, J., and R. S. Stein (1989), Coseismic folding, earthquake recurrence, and the 1987 source mechanism at Whittier Narrows, Los Angeles Basin, California, *J. Geophys. Res.*, *94*, 9614–9632.

McGill, S. F. (1998), Summary of neotectonic slip-rate studies of the Garlock and Owl Lake fault zones, *San Bernardino County Mus. Assoc. Q.*, *45*, 88–90.

McGill, S., and T. Rockwell (1998), Ages of late Holocene earthquakes on the central Garlock fault near El Paso Peaks, California, *J. Geophys. Res.*, *103*, 7265–7279.

McGill, S., and K. Sieh (1993), Holocene slip rate of the central Garlock fault in the southeastern Searles Valley, California, *J. Geophys. Res.*, *98*, 14,217–14,231.

Miller, M. M., D. J. Johnson, T. H. Dixon, and R. K. Dokka (2001), Refined kinematics of the Eastern California shear zone from GPS observations, 1993–1998, *J. Geophys. Res.*, *106*, 2245–2263.

Murray, J. R., P. Segall, and P. Cervelli (2001), Inversion of GPS data for spatially variable slip-rate on the San Andreas Fault near Parkfield, CA, *Geophys. Res. Lett.*, *28*, 359–362.

Parsons, T. (2002), Global Omori law decay of triggered earthquakes: Large aftershocks outside the classical aftershock zone, *J. Geophys. Res.*, *107*(B9), 2199, doi:10.1029/2001JB000646.

Parsons, T., R. S. Stein, R. W. Simpson, and P. A. Reasenberg (1999), Stress sensitivity of fault seismicity: A comparison between limited-offset oblique and major strike-slip faults, *J. Geophys. Res.*, *104*, 20,183–20,202.

Petersen, M. D., and S. G. Wesnousky (1994), Fault slip rates and earthquake histories for active faults in southern California, *Bull. Seismol. Soc. Am.*, *85*, 1608–1649.

Pollitz, F. F., and I. S. Sacks (1992), Modeling of postseismic relaxation following the great 1857 earthquake, southern California, *Bull. Seismol. Soc. Am.*, *82*, 454–480.

Pollitz, F. F., and I. S. Sacks (1997), The 1995 Kobe, Japan, earthquake: A long-delayed aftershock of the offshore 1944 Tonankai and 1946 Nankaido earthquakes, *Bull. Seismol. Soc. Am.*, *87*, 1–10.

Richards-Dinger, K. B., and P. M. Shearer (2000), Earthquake locations in southern California obtained using source-specific station terms, *J. Geophys. Res.*, *105*, 10,939–10,960.

Roering, J. J., M. L. Cooke, and D. D. Pollard (1997), Why blind thrust faults don't propagate to the earth's surface: Numerical modeling of coseismic deformation associated with thrust-related anticlines, *J. Geophys. Res.*, *102*, 11,901–11,912.

Ruff, L., and B. W. Tichelaar (1996), What controls the seismogenic plate interface in subduction zones?, in *Subduction Top to Bottom*, *Geophys. Monogr. Ser.*, vol. 96, edited by G. E. Bebout et al., pp. 105–111, AGU, Washington, D. C.

Rymer, M. J., K. J. Kendrick, J. J. Lienkaemper, and M. M. Clark (1990), The Nuñez fault and its surface rupture during the Coalinga earthquake sequence, in *The Coalinga, California, Earthquake of May 2, 1983*, edited by M. J. Rymer and W. L. Ellsworth, *U.S. Geol. Surv. Prof. Pap.*, *1487*, 299–318.

Salyards, S. L., K. E. Sieh, and J. L. Kirschvink (1992), Paleomagnetic measurement of nonbrittle noseismic deformation across the San Andreas Fault at Pallett Creek, *J. Geophy. Res.*, *97*, 12,457–12,470.

Savage, J. C., W. Gan, and J. L. Svarc (2001), Strain accumulation and rotation in the eastern California shear zone, *J. Geophys. Res.*, *106*, 21,995–22,007.

Seeber, L., J. G. Armbruster, W.-Y. Kim, N. Barstow, and C. Scharnberger (1998), The 1994 Cacoosing Valley earthquakes near Reading Pennsyl-

vania: A shallow rupture triggered by quarry unloading, *J. Geophys. Res.*, *103*, 24,505–24,521.
Shearer, P. M. (1997), Improving local earthquake locations using the L1 norm and waveform cross correlation: Application to the Whittier Narrows, California, aftershock sequence, *J. Geophys. Res.*, *102*, 8269–8283.
Sieh, K. E. (1978), Slip along the San Andreas fault associated with the great 1957 earthquake, *Bull. Seismol. Soc. Am.*, *68*, 1421–1448.
Stein, R. S. (1999), The role of stress transfer in earthquake occurrence, *Nature*, *402*, 605–609.
Stein, R. S. (2003), Earthquake conversations, *Sci. Am*, *288*(1), 72–79.
Stein, R. S., and G. E. Ekström (1992), Seismicity and geometry of a 110-km long blind thrust fault: 2. Synthesis of the 1982–1985 California earthquake sequence, *J. Geophys. Res.*, *97*, 4865–4883.
Stein, R. S., and W. Thatcher (1981), Seismic and aseismic deformation associated with the 1952 Kern County, California, earthquake and the relationship to the Quaternary history of the White Wolf fault, *J. Geophys. Res.*, *86*, 4913–4928.
Stein, R. S., and R. S. Yeats (1989), Hidden earthquakes, *Sci. Am*, *260*, 48–57.
Stein, R. S., G. C. P. King, and J. Lin (1994), Stress triggering of the 1994 $M = 6.7$ Northridge, California, earthquake by its predecessors, *Science*, *265*, 1432–1435.
Taylor, M. A. J., G. Zheng, J. R. Rice, W. D. Stuart, and R. Dmowska (1996), Cyclic stressing and seismicity at strongly coupled subduction zones, *J. Geophys. Res.*, *101*, 8363–8381.
Taylor, M. A. J., R. Dmowska, and J. R. Rice (1998), Upper plate stressing and seismicity in the subduction earthquake cycle, *J. Geophys. Res.*, *103*, 24,523–24,542.
Toda, S., and R. S. Stein (2002), Response of the San Andreas fault to the 1983 Coalinga-Nuñez earthquakes: An application of interaction-based probabilities for Parkfield, *J. Geophys. Res.*, *107*(B6), 2126, doi:10.1029/2001JB000172.
Toda, S., and R. S. Stein (2003), Toggling of seismicity by the 1997 Kagoshima earthquake couplet: A demonstration of time-dependent stress transfer, *J. Geophys. Res.*, *108*(B12), 2527, doi:10.1029/2003JB002527.
Toppozada, T. R., C. R. Real, and D. L. Parke (1981), Preparation of isoseismal maps and summaries of reported effects for pre-1900 California earthquakes, *Calif. Div. Mines Geol. Open File Rep.*, *81-11 SAC*, 1–182.
Wang, J. C., C. F. Shieh, and T. M. Chang (2003), Static stress changes as a triggering mechanism of a shallow earthquake: Case study of the 1999 Chi-Chi (Taiwan) earthquake, *Phys. Earth Planet. Inter.*, *135*, 17–25.
Wang, W. H. (2000), Static stress transfer and aftershock triggering by the 1999 Chi-Chi earthquake in Taiwan, *Terr. Atmos. Ocean. Sci.*, *11*, 631–642.
Wang, W. H., and C. H. Chen (2001), Static stress transferred by the 1999 Chi-Chi, Taiwan, earthquake: Effects on the stability of the surrounding fault systems and aftershock triggering with a 3D fault-slip model, *Bull. Seismol. Soc. Am.*, *91*, 1041–1052.
Weldon, R. J., II, and K. E. Sieh (1985), Holocene rate of slip and tentative recurrence interval for large earthquakes on the San Andreas fault in Cajon Pass, southern California, *Geol. Soc. Am. Bull.*, *96*, 793–812.
Zoback, M. D., et al. (1987), New evidence on the state of stress of the San Andreas fault system, *Science*, *238*, 1105–1111.

J. Lin, Department of Geology and Geophysics, Woods Hole Oceanographic Institution, Woods Hole, MA 02543, USA. (jlin@whoi.edu)
R. S. Stein, U.S. Geological Survey, Menlo Park, CA 94025, USA. (rstein@usgs.gov)